Nucl. Fusion 51 (2011) 103031 (10pp) doi:10.1088/0029-5515/51/10/103031

Dynamical evolution of pedestal parameters in ELMy H-mode in the National Spherical Torus Experiment

A. Diallo[1], R. Maingi[2], S. Kubota[3], A. Sontag[2], T. Osborne[4], M. Podestà[1], R.E. Bell[1], B.P. LeBlanc[1], J. Menard[1] and S. Sabbagh[5]

[1] Princeton Plasma Physics Laboratory, Princeton University, NJ, USA
[2] Oak Ridge National Laboratory, Oak Ridge, TN, USA
[3] Department of Physics and Astronomy, University of California, Los Angeles, CA, USA
[4] General Atomics, San Diego, CA, USA
[5] Applied Physics Department, Columbia University, New York, NY, USA

E-mail: adiallo@pppl.gov

Received 3 March 2011, accepted for publication 15 June 2011
Published 16 September 2011
Online at stacks.iop.org/NF/51/103031

Abstract

Characterizations of the pedestal parameter dynamics throughout the edge localized mode (ELM) cycles are performed on the National Spherical Torus Experiment (NSTX, (Ono *et al* 2000 *Nucl. Fusion* **40** 557)). A clear buildup of the pedestal height between ELMs is observed for three different plasma currents. This buildup tends to saturate at low and medium plasma currents. Similarly, the pedestal width increases with no clear evidence of saturation during an ELM cycle. The maximum pedestal gradient increases as a function of plasma current, reaches a nominal value after the ELM crash, and remains constant until the end of the ELM cycle. The pedestal height just prior to the onset of ELM is shown to increase quadratically with plasma current. The pedestal width (Δ) scales as $\Delta = 0.17\sqrt{\beta_\theta^{\rm ped}}$ with the poloidal β at the top of the pedestal. Coherent density fluctuations strongly increasing at the plasma edge are observed to be maximum after the ELM crash and to decay during the rest of the ELM cycle. Finally, the evolution of the pedestal height and width during the ELM cycle as well as the scaling with $I_{\rm p}$ of the pedestal pressure prior to the onset ELM are found to be qualitatively consistent with the peeling–ballooning theory.

(Some figures in this article are in colour only in the electronic version)

1. Introduction

A successful operation of fusion reactors such as ITER [1] will require establishing a sufficiently high pressure at the top of the pedestal (referred to as pedestal height) during H-mode discharges. This is mainly due to the coupling between pedestal pressure and core fusion power. In addition, edge localized mode-(ELM)-induced energy loss must be restricted to less than a 1% reduction of the pedestal stored energy in ITER to meet the heat load requirements on the plasma-facing components (PFC) [2].

A defining feature of the H-mode is the existence, near the plasma boundary, of a transport barrier generating an H-mode pedestal. This pedestal can be quite narrow in width and is interpreted as the interface between two regions during high confinement (H-mode): the core plasma and the scrape-off layer (SOL). These two regions are governed by different physical mechanisms inherent in the wide range of spatial and temporal scales and also in the presence of sources and sinks of particles. A large pedestal pressure has been found to improve the energy confinement, as seen in DIIID [3] and JT-60U [4]. Predictions of the pedestal pressure required for a ratio of auxiliary heating to thermal power (i.e. Q) of 10 such as ITER is challenging without an accurate model of the edge pedestal and of its self-consistent coupling to the core plasma. Significant efforts have been undertaken in simulations using the multi-mode (MM), Weiland, IFS/PPPL and GLF23 theory-based transport models (see [5] and references therein), which showed that the pedestal ion temperatures ($T_{\rm i}^{\rm ped}$) required for achieving $Q = 10$ in ITER range between 3 to 5 keV, compatible with ITER $T_{\rm i}^{\rm ped}$ projections [6]. From the experimental point of view, significant research from multiple tokamaks looking into pedestal parameter scalings with plasma parameters are currently being undertaken and the current status and results of these experiments have been summarized in a review paper [7].

It is well known that in ELMy H-mode, the core confinement and stored energy increase as the pedestal pressure and its gradient rise until a threshold, and therefore an upper limit, is reached. This limiting threshold appears to be controlled by combinations of magnetohydrodynamic dynamics (MHD) instabilities and transport physics. While there is no accepted transport mechanism explaining the residual electron heat transport in the pedestal, linear MHD through the peeling–ballooning theory, however, provides a good description to the upper limit on the pedestal pressure.

The peeling–ballooning theory describes instabilities driven by both pressure and edge current gradients [8]. Based on this theory, the onset of an ELM is driven by a critical pressure gradient ($\nabla p_{\rm crit}$) at a given pedestal width, which in turn peaks the bootstrap current. Making the assumption that the maximum pedestal pressure (resulting in an upper limit) can be written in terms of the pedestal width $\Delta_{\rm p}$ and critical pressure gradient as $\Delta_{\rm p} * \nabla p_{\rm crit}$, one can argue that one aspect of the peeling ballooning theory effectively provides the maximum pedestal height which is more accurately quantifiable than $\nabla p_{\rm crit}$ prior to the onset of ELM. The other aspect of the peeling–ballooning theory is related to the edge current gradient. In addition to the local parameters (e.g. $\nabla p_{\rm crit}$), the peeling–ballooning theory is sensitive to the radial extent of the associated modes, and the overall size of the pedestal. The upper limit of the pedestal pressure is thought to be reached just prior to the onset of an ELM. Once an ELM is triggered, filamentary bursts [9] of energy and particles are transported from the vicinity of the pedestal to the SOL thereby relaxing the pedestal pressure and edge current gradients to a stable regime. We refer to pedestal height as the total thermal (ion and electrons) pressure at the top of the pedestal ($P_{\rm ped}$).

Recent DIIID [10, 11] results from a model study based on the peeling–ballooning theory showed that the pedestal width scales with the pedestal poloidal beta $\beta_\theta^{\rm ped} = 2\mu_0 P_{\rm ped}/B_\theta^2$. Here $B_\theta = \mu_0 I_{\rm p}/L_{\rm p}$ is the averaged poloidal magnetic field at the pedestal top and $L_{\rm p}$ the circumference of the last closed flux surface. In the experiments testing the model, the pedestal width was approximated as $(\Delta_{n_{\rm e}} + \Delta_{T_{\rm e}})/2$, where $\Delta_{n_{\rm e}}$ and $\Delta_{T_{\rm e}}$ represent electron density and temperature widths, respectively. ASDEX Upgrade [12], on the other hand, found that $\Delta_{n_{\rm e}}$ is independent of $\beta_\theta^{\rm ped}$ and the $\Delta_{T_{\rm e}}$ scaling with $\sqrt{\beta_\theta^{\rm ped}}$ cannot be excluded within error bars. The latter correlation appears to be consistent with observations from other tokamaks. More specifically, on JT-60, Urano *et al* [13] found through mass scans using hydrogen and deuterium that the pedestal width scales with $\rho^{*0.2}\sqrt{\beta_\theta^{\rm ped}}$. Here $\rho^* \propto T_{\rm i}^{\rm ped}/aB_\theta^{\rm ped}$ (a is the minor radius). MAST has reported similar scalings where $\Delta_{T_{\rm e}}$ scaled weakly with ρ^* but correlated with $\sqrt{\beta_\theta^{\rm ped}}$ [14]. The above observations from multiple tokamaks show a mix of trends in the pedestal height-width scalings, which suggests the existence of hidden variables. Extension of these scalings to low aspect-ratio tokamaks are necessary for a wide plasma parameter coverage. In addition, fluctuation measurements in the pedestal region during the inter-ELM phase are needed for a complete understanding of the pedestal structure dynamics.

The H-mode pedestal in National Spherical Torus Experiment (NSTX) was first described in the work of Maingi *et al* [15]. In that work, analysis of the pressure profiles in NSTX showed that the pedestal stored energy represents between 25% and 33% of the total plasma stored energy. Furthermore, the pedestal stored energy was found to agree with the multi-machine scaling relation reported in Cordey [16]. In NSTX, multiple intrinsic ELMs ranging from large to small have routinely been observed [15]. The ELM sizes are typically given as the ratio of ejected stored energy to either the pedestal or the total stored energy. Giant type I ELMs can eject up to 30% of the stored energy. Small ELMs (type V see [17]), however, have less than a 1% effect on the total stored energy, making them difficult to measure via equilibrium reconstructions.

All the previously quoted research on NSTX was performed with boronized carbon PFCs. Recently lithiumization was introduced as a wall conditioning technique. Lithium evaporations on part of the PFC walls resulted in reductions in the frequency and amplitude of ELMs [18], including complete ELM suppression for periods of up to 1.2 s. The ELM suppression is attributed to modification of the edge stability [19]. There is a minimum amount of lithium required for complete ELM suppression. For lithium evaporation below this minimum amount, ELMs are still observed. Thus, to access ELMy regimes and to ensure discharge reproducibility, low levels of Li coating (<100 mg) are typically applied to the bottom divertor between discharges in this set of experiments.

In this work, we first show evolution of the pedestal parameters (e.g. height, width, gradient) during an ELM cycle as a function of plasma current $I_{\rm p}$ at constant plasma shaping with toroidal magnetic field B_φ varying within 10%. Then we show the total pedestal pressure scales with $I_{\rm p}^2$. In addition, the pedestal width scales with $\sqrt{\beta_\theta^{\rm ped}}$. These scalings provide a good description of NSTX data over a wide range of $I_{\rm p}$. Finally, we examine correlations between the pedestal width and edge fluctuations. More specifically, we analyse the density fluctuations near the plasma edge during an ELM cycle, and compare the fluctuation levels with pedestal width evolution. Initial results show that these density fluctuations appear to be uncorrelated with the ELM cycle.

The rest of this paper is organized into four sections. Section 2 describes the experimental details and the profile analysis techniques needed to systematically obtain the pedestal structure scaling results. Evolution of the pedestal parameters during an ELM cycle and scalings with global parameters are discussed in section 3. Analysis of fluctuations during an ELM cycle is presented in section 4. Finally, section 5 presents a summary.

2. Experimental description and profile analysis technique

Experiments were carried out on the NSTX, a medium-sized low aspect-ratio spherical torus (ST) of major radius $R \sim 0.85$ m, minor radius $a \leqslant 0.67$ m and $B_\varphi \leqslant 0.55$ T. The experiments described here are performed using neutral beam injection (NBI) heating with power ranging from 4 to 6 MW. The discharges studied use a marginally double-null divertor configuration, with the plasma slightly biased down

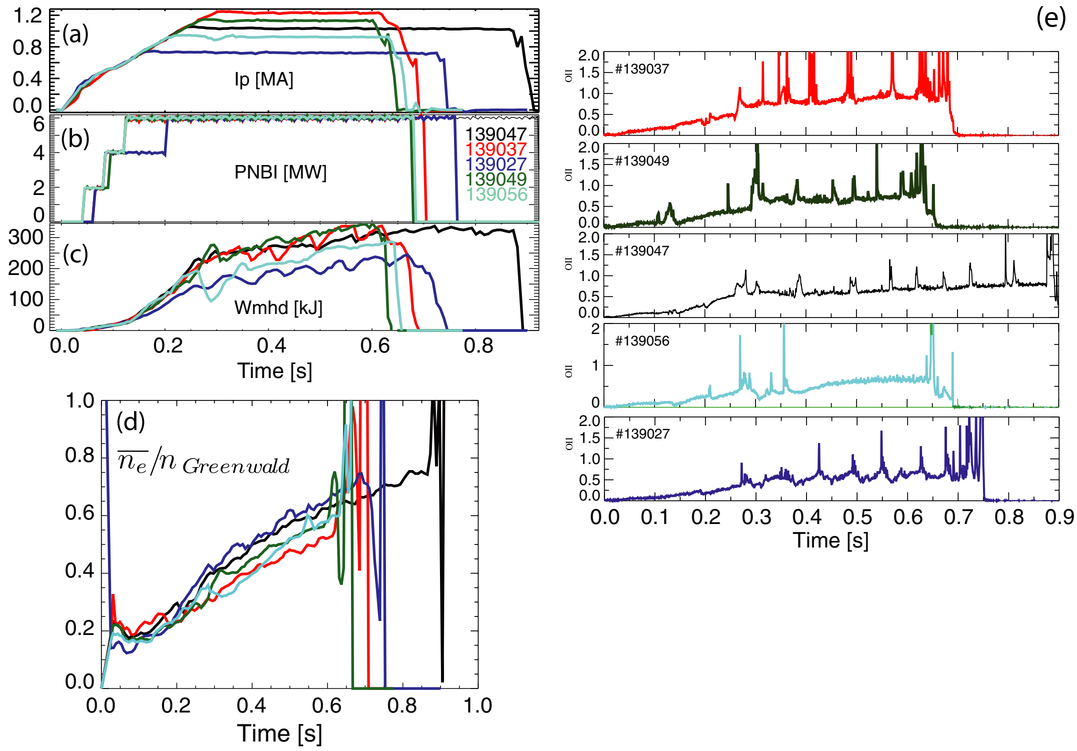

Figure 1. Discharges characteristics: (*a*) plasma currents. (*b*) Injected power. (*c*) Total stored energy showing dips associated with ELMs. (*d*) The Greenwald density fraction. (*e*) Divertor O-II signals clearly showing ELMs. Note the divertor O-II signals can be used in *lieu* of the D_α.

($\delta_r^{sep} \sim -5$ mm, where $\delta_r^{sep} \sim$ is the radial distance between the two X-points mapped to the outer mid-plane), and the bottom triangularity $\delta_{bot} \sim 0.6$. The upper triangularity was typically kept at 0.4 and the elongation κ was kept between 2.3 and 2.4. Figure 1 shows the NBI power, I_p, total stored energy (W_{mhd}), and divertor O-II (proxy for the D_α) signals of the discharges examined in this paper. The shape parameters (e.g. δ, κ) were held constant and the magnetic field was varied from 0.5 to 0.55 T. To target ELMy discharges for studies reported here, a total of 50 mg of lithium was deposited on the bottom divertor plates between discharges. The key diagnostics utilized to characterize the pedestal parameters are the mid-plane Thomson scattering system for n_e and T_e sampled at 60 Hz [23], the C^{6+} charge-exchange recombination spectroscopy [24] for providing the carbon density and ion temperature T_i with a 10 ms time resolution, and the divertor O-II and the D_α filter scopes for identifying ELMs. In this work, we use the divertor O-II signal instead of the D_α.

In this work, analysis of the evolution of the pedestal structure during an ELM cycle is presented. We characterize the evolution of the radial profiles between ELMs by reconstructing composite profiles synchronously with multiple ELMs. Here, we focus on type I ELMs of typical frequency ranging between 20 and 70 Hz and characterized by large spikes on the divertor O-II signal as indicated in figure 2(*a*). The radial profiles of density, temperature and consequently the pressure are first mapped in normalized poloidal flux coordinates ($\psi_n = (\psi_c - \psi)/(\psi_c - \psi_{sep})$, where ψ_c and ψ_{sep} represent the flux at the core and at the separatrix, respectively), and then collected during inter-ELM periods: this can be regarded as a correlated sampling approach. The equilibrium reconstruction has a 10 ms time resolution, however for the purpose of the profile reconstruction, the equilibrium is down-sampled to match the Thomson scattering sample frequency (i.e. 60 Hz).

An example of this correlated sampling for the n_e profile is shown in figure 2(*b*) where the dashed line represents the best fit using a modified hyperbolic tangent function that parametrizes the pedestal height and width [25]. This widely used analytic function fits the steep gradient region in the pedestal, reduces sensitivity to noise in individual data points, and provides a systematic way to represent pedestal structure [26]. The electron profiles (n_e and T_e) are fitted using a modified hyperbolic tangent defined as

$$\frac{\alpha - \alpha_0}{2}\,\frac{(1 - a_1\zeta)e^{\zeta} - e^{\zeta}}{e^{\zeta} + e^{-\zeta}} + \frac{\alpha + \alpha_0}{2}.$$

where α and α_0 represent the pedestal height and the offset (shown in the inset of figure 2), respectively. $\zeta = 2(\psi_n^{sym} - \psi_n)/\Delta$, ψ_n^{sym} and Δ represent the symmetry point and the width, respectively. The ion profiles exhibit less of steep gradients than the electron profiles and hence cannot be fitted using the modified tanh function. They are adequately fitted using cubic splines.

The profile fits are performed around sliding temporal windows of 20% width to capture details of the inter-ELM dynamics. For example, we represent a window between 30% and 50% of an ELM cycle by its midpoint, which in this case is 40%. With this defined proxy, n_e or T_e *prior to* and *after* an ELM crash are identified as 90% and 30% of an ELM cycle, respectively. On average three profiles are used to constrain each sliding window. Figure 3 shows examples of profiles for

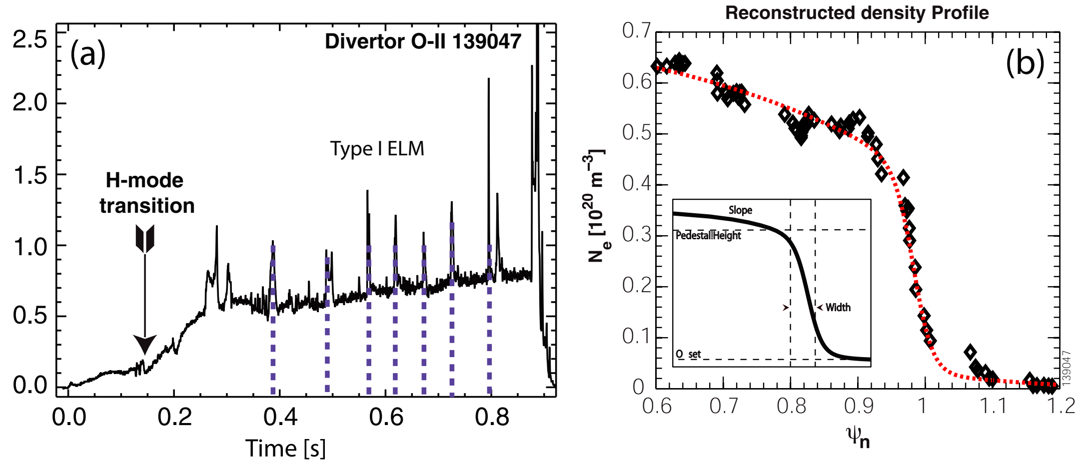

Figure 2. (*a*) The divertor O-II signals with large type I ELMs. The dashed vertical bars indicate the ELM times. (*b*) Example of a composite profile, in normalized flux ψ_n, of the electron density associated with type I ELM in (*a*). Diamonds represent the data points and the broken line the best fit using a modified hyperbolic tangent. The inset plot illustrates the parametrizations utilized for the fits (see the text for details). Typical vertical error bars ~5%. Larger error bars occur in the far SOL.

ions and electrons with associate fits (from $\psi_n = 0.7$), where the electron pedestal density, temperature, and subsequently pressure are higher prior to the onset of ELMs than just after, which clearly indicates an increase in the total pressure prior to the onset of an ELM. In addition, we observe an inward shift of the top of the pedestal hinting at an increase in the pedestal width. For the rest of the text, the pedestal parameters refer to those of the total pressure derived using a composite of n_e, T_e, n_i, T_i profiles. This composite is subsequently fit using the modified tanh function given in the above equation. The resulting fit yields an estimate of the pedestal width (Δ) from which a gradient (α/Δ) can be determined. The error in the fit in combination with an estimate of the scatter around the fit yields estimates on the error of the pedestal parameters.

3. Pedestal structure evolution during an ELM cycle and scaling studies

Based on linear ideal MHD stability theory, it has been suggested that ELMs are associated with both ballooning [27] and kink or peeling modes [28, 29], or with a combination of both referred to as peeling–ballooning modes [8, 30]. The latter mode taps its free energy from both the pressure gradient and the current density [8]. NSTX ELMy discharges, however, have been shown to be kink/peeling unstable [20–22]. ELMs are thought to be triggered at a critical pedestal pressure gradient or edge current gradient. In this section, we show results of measurements of the pedestal structure on NSTX for various I_p during an ELM cycle.

Pedestal parameters evolution through an ELM cycle. The total pressure (i.e. ions and electrons) evolution at the top of the pedestal during various stages of an ELM cycle for three cases of plasma current is shown in figure 4. The ELM frequencies vary between 20 and 70 Hz with no systematic trend as a function of I_p. We observe a clear buildup of the pedestal pressure before the onset of ELMs for these cases (low, medium, and high I_p all at the same toroidal field ~0.5 T) similar to observations in MAST [31] and AUG [32]. In the low and medium I_p cases, we observe a saturation late in the ELM cycle of the pedestal height in contrast to the high current case where the pedestal height increases until the onset of the ELM. In addition, figure 4 shows a factor of three increase in pedestal height during the ELM cycle for the high plasma current case: this is similar to DIIID where a factor of four increase of the inter-ELM pedestal pressure was observed [33]. The saturation late in the ELM cycle is in contrast to observations in DIIID [33], where the electron pedestal pressure saturates in the early phase, e.g. 20–50% of the ELM cycle.

Figure 5(*a*) indicates, for the case of $I_p = 1.2$ MA and to a lesser extent for the case of 0.7 MA, that the pedestal width increases until the onset of an ELM to a nominal value of ~2 cm (0.085[ψ_n]). For the medium I_p case, only one point is included in the early stage of the ELM cycle as the remaining points have error bars too large to allow for meaningful comparison. We note that the widening of the pedestal during the ELM cycle is qualitatively consistent with the phenomenology of transport barrier inward expansion [34, 35]. An analytic model based on this phenomenology predicts that the rise of the pedestal width results from an inward propagation from the edge of the pedestal pressure front into the core plasma [34], which implies an increase in the pedestal pressure width.

Figure 5(*b*) shows the maximum pressure gradient for various parts of an ELM cycle. There is an increase in the maximum pressure gradient with I_p. Furthermore, we observe that the maximum pressure gradient remains constant within error bars during the ELM cycle. This lack of variation in the maximum pressure gradient is consistent with recent observations in both AUG [36] and DIIID [7, 33], where the maximum pressure gradient initially increases and is limited at an early phase of the ELM cycle. In our case, the increase in the pressure prior to its saturation (before the 20% of the ELM cycle) could not be resolved. Hence, in view of this saturation prior to the ELM crash, the pressure gradient appears to play a weak role in the triggering of an ELM. In the framework the peeling–ballooning physics, it is conceivable that the edge current could play a role just prior to the ELM crash.

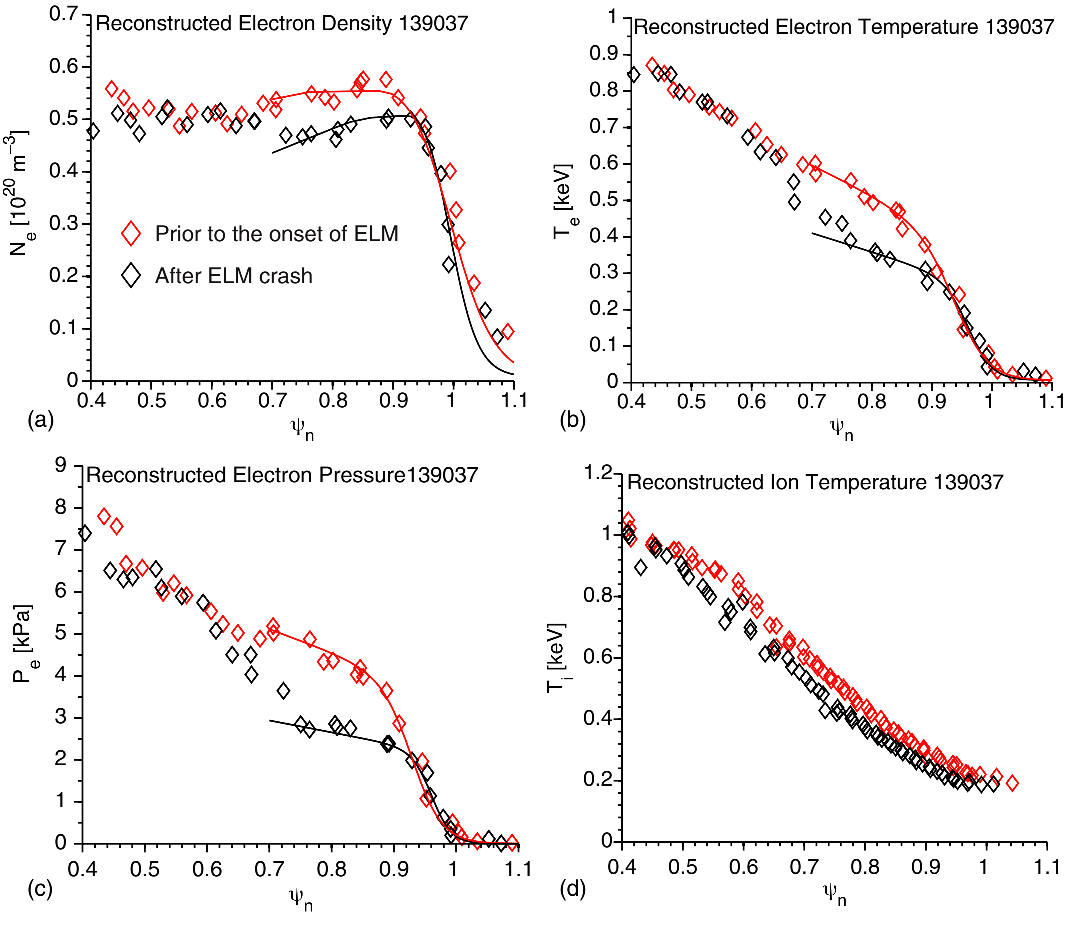

Figure 3. Example of ELM based reconstruction profiles prior to the onset and after an ELM: (*a*) electron density; (*b*) electron temperature; (*c*) electron pressure and (*d*) ion temperature. Error bars in the range of 3% are typical for n_e, and in range of 4% to 5% for T_e and P_e.

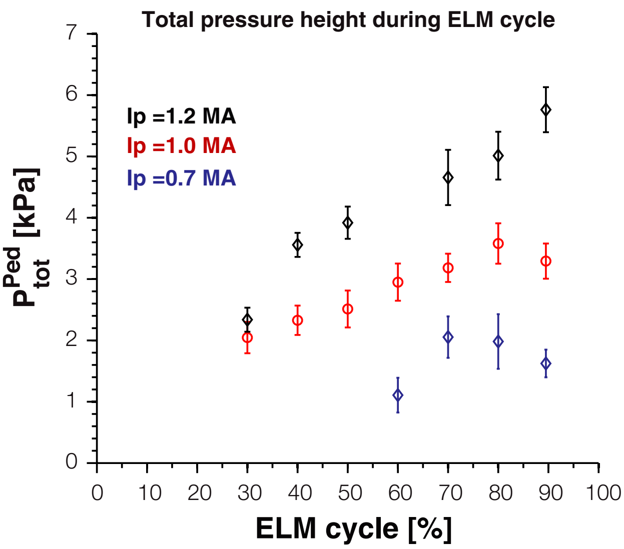

Figure 4. Total pressure buildup during ELM cycle, for three cases of I_p; all other parameters are kept constant. The ELM frequency ranges from 20 to 70 Hz.

Thus, we have shown that the pedestal maximum is a limit and can hypothesize the critical gradient is recovered very soon after the ELM crash leaving the pedestal height and width, and the edge current as key players in the onset of the ELMs. Observations of the pedestal height evolution for various plasma currents are consistent with observations made in high R/a tokamaks such as DIIID [37], and provide additional opportunities for extending predictive pedestal structure models to ST.

Pedestal width scaling with plasma current, magnetic field and poloidal β: Correlations between the pedestal width and β_θ^{ped} have been observed on many tokamaks (e.g. JT-60U [4], MAST [14], and see [38] for DIIID and CMOD). Independent correlations, however, between the width and ρ^* and width and β_θ^{ped} have been difficult to assess. In JT-60U, to separate the dependence between ρ^* and β_θ, experiments in hydrogen and deuterium were carried out keeping β_θ and ν^* fixed in type I ELMy discharges. It was found that the pedestal width dependence on ρ^* is weak and that the ion temperature pedestal width was found to scale with $\rho^{*0.2}\sqrt{\beta_\theta^{ped}}$ [13] and similar results on the pedestal width (i.e. $(\Delta_{T_e} + \Delta_{N_e})/2$) in DIIID [10] showed a weaker dependence in ρ^* but scaling with $\sqrt{\beta_\theta^{ped}}$. The DIIID pedestal width scaling was observed to be in agreement with the EPED predictive model (the reader is referred to Snyder *et al* [39] for details on the EPED model). EPED combines a pedestal width constraint, based on expectations from the onset of strong electromagnetic kinetic ballooning mode (KBM) turbulence near a critical value of the pressure gradient, with peeling–ballooning stability to

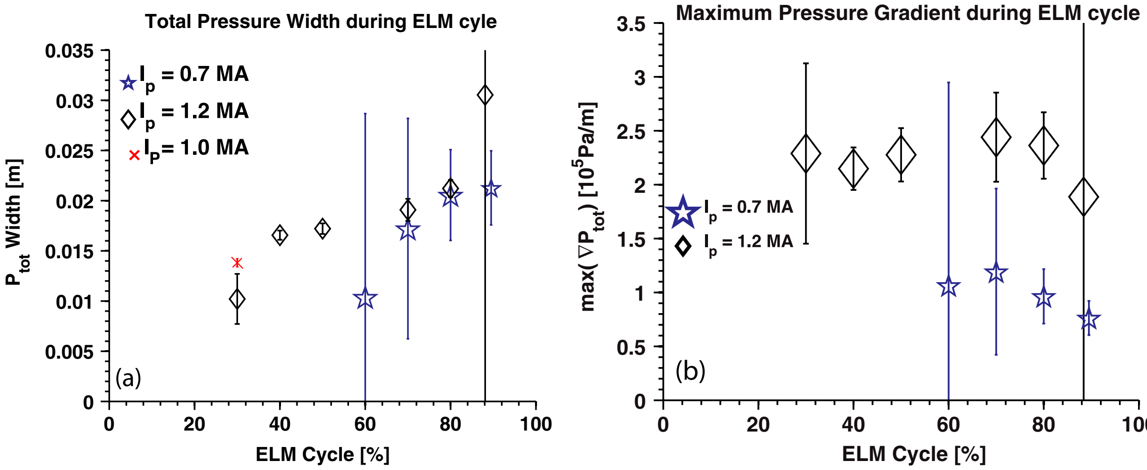

(a) Width evolution (b) Maximum pressure gradient evolution

Figure 5. (*a*) Pressure width evolution during an ELM cycle for three values of plasma current. Stars (★) indicate the pedestal width for the low plasma current case; the diamond (♦), the high plasma current case and the cross (×) the medium current case. (*b*) The maximum pressure gradient for the low and high current remains unchanged (within errorbar) during an ELM cycle.

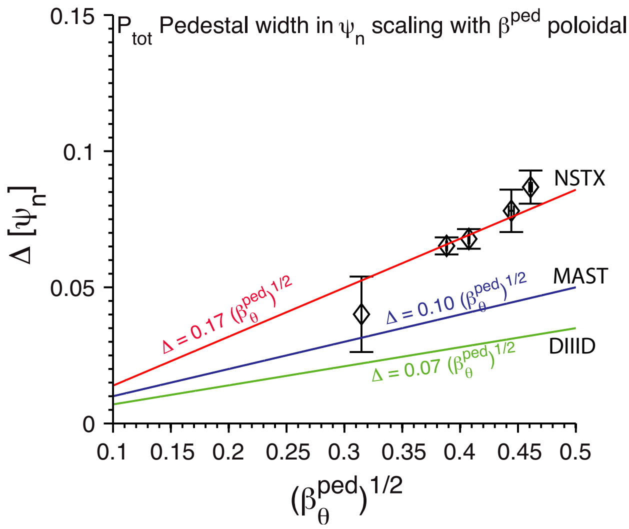

Figure 6. The pedestal width in ψ_n scaling with the pedestal poloidal β and the associated best fit. This width scaling effectively provides a relation between the width and the height of the pedestal (see text for details). Shown also are the fits for MAST and DIIID for comparison.

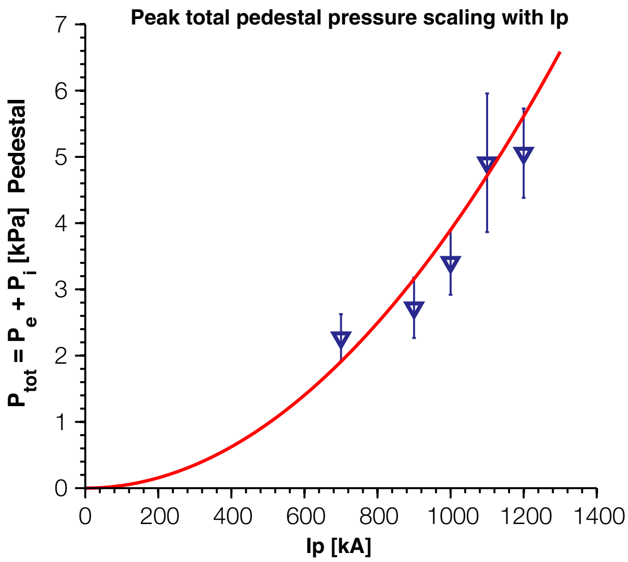

Figure 7. Pedestal height scaling with I_p: collecting the pedestal pressure at the onset of ELMs, we show that the pedestal height scales with I_p^α, where $2.0 \leqslant \alpha \leqslant 2.6$ with a reduced $\chi^2 \sim 0.63$.

yield a predictive model on the pedestal height and width. Furthermore, based on the KBM dispersion relation, the onset of the KBM leads to weak or no dependence of the width on other normalized parameters.

In NSTX, we observe no systematic trends between the pedestal width and ρ^* (evaluated at the electron pedestal temperature), which is not inconsistent with the KBM arguments. On the other hand, figure 6 shows a clear dependence of the pedestal width prior to the type I ELM onset (e.g. the last 20% of an ELM cycle) of type I ELM on β_θ^{ped}. The width scales with $\sqrt{\beta_\theta^{ped}}$, with a best fit equation being $\Delta = 0.17(\beta_\theta^{ped})^{1/2}$. This pedestal width correlation of the type '$\Delta = c(\beta_\theta^{ped})^{1/2}$' is consistent with experimental observations in DIIID and MAST, except the fitting coefficient c in NSTX is slightly larger than that of MAST [14] and 2.4 times greater than that of DIIID [10]. In summary, the coefficient appears to be overall larger in ST than in high aspect-ratio tokamaks pointing to a different type of coupling of the pedestal width and height in STs. The difference in values of c in STs remains unclear. Furthermore, this scaling provides the necessary ingredients for testing EPED in STs. Note that EPED was initially developed for large aspect-ratio tokamaks. Testing of a version of EPED supporting low aspect-ratio tokamaks will be the subject of future work.

To further characterize the pedestal, we examine the total pedestal pressure dependence with global parameters such as I_p. We compile the total pedestal pressure during the last 20% of an ELM cycle. Figure 7 shows a near quadratic (within error bars) increase in the pedestal height prior to the ELM onset (e.g. 90% ELM cycle) with I_p. Note that the toroidal field was 10% higher for $I_p = 900$ kA and 1.1 MA than that of $I_p = [1.2, 1.0, 0.7]$ MA.

Initial test of the effects of B_φ on this scaling showed limited effects on the pedestal height. The test was performed over a small range of B_φ with ELMy discharges and a larger range of ELM-free discharges, where no discernible effect on the pedestal height could be found. A more stringent test will be performed using a much larger set of ELMy discharges to be obtained over a wider range of B_φ in a future experimental campaign.

The above scaling studies show that I_p has a dominant effect in determining the pedestal height compared with B_φ. Similar scaling consistent with I_p^2 scaling has been observed in CMOD [40] on the 'Enhanced D_α' H-mode datasets. DIIID, however, has reported a linear scaling of the electron pedestal height with I_p (see figure 3(*c*) in [37]), which can arguably change once the ion pedestal height is included. The I_p^2 dependence of the pedestal pressure has been suggested by Lingertat *et al* [41] as a manifestation of the ballooning instability. While such scaling is expected in JET [42] discharges, recent NSTX stability analysis using ELITE [43, 44] have shown that ELMy discharges are at the kink/peeling boundary [21]. Similarly, on CMOD, stability analyses have demonstrated operation above the ballooning stability limit, even though the pedestal scaling with $I_p^{2\leqslant\alpha\leqslant 2.6}$ was also observed. The discrepancy between stability analysis and observed scaling as a manifestation of ballooning instability points to the existence of other mechanisms (e.g. transport) playing a role.

4. Density fluctuation analysis during an ELM cycle

The characterization of the evolution of the density fluctuations during an ELM cycle is motivated by a recent hypothesis where it was proposed that the onset of a KBM near a critical value of the pressure gradient sets the pedestal width [39]. This ballooning type mode is predicted to have its real frequency near $\omega_{pi}^* \sim 30$ kHz [45] assuming $k_\theta\rho_i$ in the vicinity of 0.3, and with $\omega_{pi}^* = 0.5k_\theta\rho_i v_{thi}/L_{ni}(1+\eta_i)$. Here, L_{ni} is the ion density gradient scale length, v_{thi} is the ion thermal velocity, and η_i the ratio of density to temperature scale lengths. Recent gyrokinetic simulations of a representative NSTX high-beta discharge have shown the transition between distinct ITG and KBM modes to an hybrid ITG/KBM mode at large pressure gradient [46] and at $r/a = 0.7$ further motivating the need to identify the KBM experimentally. KBMs are hypothesized to set the pedestal gradient, which in turn constrains both the pedestal width and height. To qualitatively test this hypothesis, we investigate correlations between the pedestal structure evolution and density fluctuations.

The density fluctuations at various stages of an ELM cycle are obtained using the 16-channel reflectometer probing the edge plasma [47]. From the complex signal (in-phase and quadrature), one obtains the phase fluctuations which can in principle be related to local density fluctuations (see [48] for a review). We then conditionally sample, based on the ELM cycle, the deduced phase signal for each channels. The resulting signal is decomposed into temporal segments of an ELM cycle (e.g. 20–40%). Such decomposition ensures that n_e measurement points are included in each temporal segment and independently for each channel.

In order to extend the analysis to the frequency domain, we cross-correlate pair-wise the segments corresponding to the same ELM cycle for various ELMs, and then apply a Fourier transformation. This approach eliminates uncorrelated fluctuations and yields a cross-power spectrum of the phase fluctuations. In addition, we average over all the ELMs present in the discharges, which further suppresses the noise ($1/\sqrt{N}$, N is the number of ELMs) to enhance the correlated components. A similar approach was successfully implemented in Diallo and Skiff [49] to pull a kinetic component of weak amplitude out of fluctuation spectra dominated by drift waves. The resulting phase fluctuation spectra are mapped into ψ_n space using the electron density fit (see figures 8(*d*)–(*f*)) and the reflectometer cutoff densities.

To estimate the local density fluctuations based on the phase fluctuations, we assume a 1D geometric optics approximation [48] where $k_r L_n \leqslant 1$, which is a reasonable assumption for the edge of the tokamak. Given this assumption, the phase fluctuation $\delta\varphi$ corresponds approximately to $\sim 2k_0 L_n \delta n_e/n_e$ as described in [48]. Here L_n is the density scale length computed from density profiles in figures 8(*d*)–(*f*), and k_0 the vacuum wavenumber at the cutoff densities. Figures 8(*a*)–(*c*) show contour plots of the cross-power spectra of the density fluctuations during the early-, mid- and late- phases of the ELM cycle. Most of cross-power spectra are localized towards the region of strong density gradients. Furthermore, the fluctuations, estimated using the phase fluctuations, increase at the very edge of the plasma away from the peak density gradients (see figure 9). Due the lack of reflectometer measurements in the SOL, it remains unclear if this increase of the fluctuations away from the peak density gradient can be ascribed to edge transport barrier phenomenon or if the increased levels of fluctuations continue into the SOL. Note a slight radial shift between the peak density gradient and the maximum density fluctuations, which we attribute to misalignment due to the equilibrium reconstructions.

The observed density fluctuations exhibit a coherent peak in the vicinity of 12 kHz at the edge of the density. The overall fluctuation level decreases prior to the onset of ELM. The characteristics of the 12 kHz coherent fluctuation observed in the density fluctuations could not be attributed to modes detected on the Mirnov signals as shown in figure 10, which indicates that either the peak density fluctuation spectra are too weak to be detected by Mirnovs or that they are electrostatic.

From the constant pressure gradient during the ELM cycle observed in figure 5(*b*) for the other two cases ($I_p = 1.2$ MA and $I_p = 0.7$ MA), one might conclude the fluctuation level provided by the pressure gradient drive remains constant during the ELM cycle. This, however, is not reflected in the observed density fluctuations. One can speculate that the quenching of the density fluctuations leads to a reduction in the particle transport during an ELM cycle which is not inconsistent with a pedestal buildup during ELM cycle. Nonetheless, the observed fluctuations suggest that they are

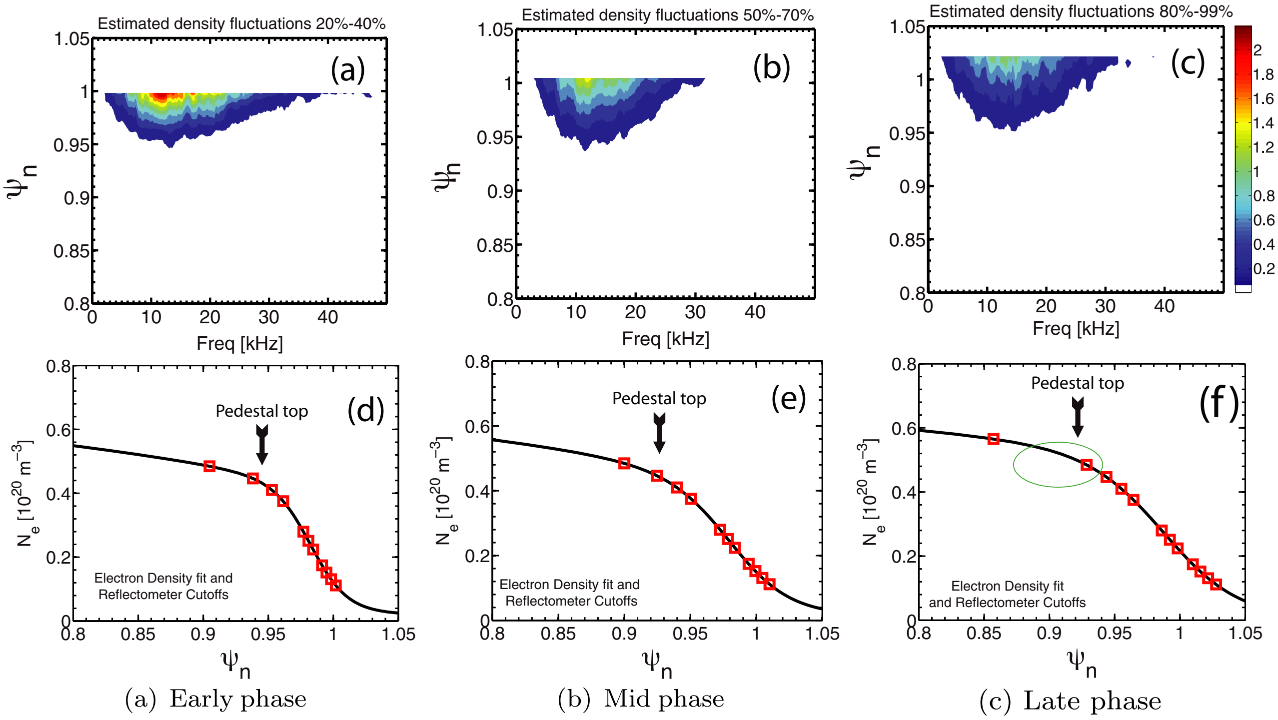

Figure 8. Estimated density fluctuations contour plots during the ELM cycle with associated density profiles during three phases of the ELM cycle for the medium plasma current case ($I_p - 1.0$ MA). The same colourbar scale is used for all three contour plots. The bottom row shows the density profiles with the squares indicating the reflectometer probing locations and the arrows pointing to the top of the pedestal.

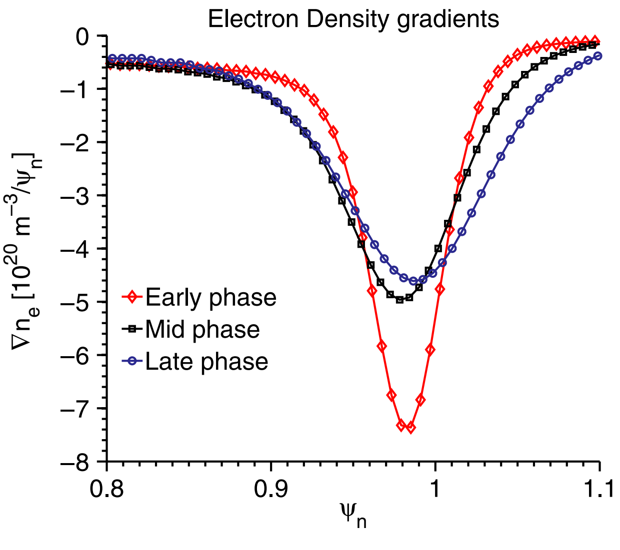

Figure 9. Density gradients obtained from fits during the three ELM phases for $I_p = 1.0$ MA.

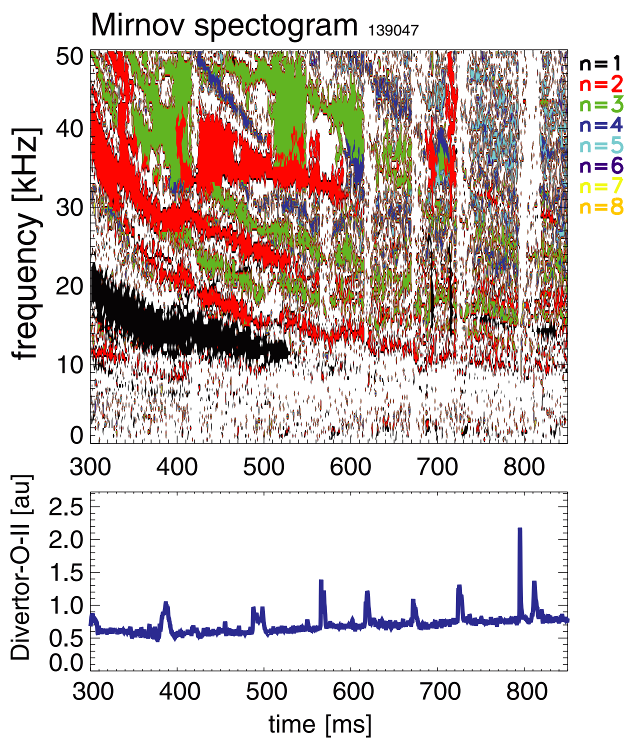

Figure 10. Top: signature of MHD activities using spectrograms from Mirnov coils with associated n-number modes. Below: corresponding divertor O-II signals showing the ELM events.

not likely to play a role in constraining the profiles inside the edge barrier.

5. Summary

In this work, we provide detailed analysis of the dynamical evolution of the pedestal parameters in NSTX NBI heated discharges with type I ELMs. Analyses of scans in I_p and B_φ at constant shape during ELM cycle have been performed. We have shown that the pedestal height and width increase during ELM cycles qualitatively consistent with the peeling–ballooning theory. The maximum gradient of the total pressure remains constant throughout the ELM cycle once a nominal gradient ($\nabla p_{\rm crit}$) is recovered immediately after the ELM crash. The saturation at $\nabla p_{\rm crit}$ early in the ELM cycle clearly indicates that the pressure gradient is unlikely a key player in triggering ELMs. Coupled with the saturated gradient is an increase in the pedestal width, which is known to be destabilizing. Assuming the peeling–ballooning theory as working model for the ELM triggering both the width expansion and edge current gradient are candidates for the triggering of the ELMs.

The pedestal height was found to scale with $I_{\rm p}^2$ similar to CMOD observations [40]. Such $I_{\rm p}^2$ dependence appears to be a manifestation of the ballooning instability [41], which would suggest that the pedestal height scaling can be ascribed to the ballooning stability. In addition, the $I_{\rm p}^2$ scaling of the pedestal height is clearly favourable for higher current machine and bodes well in NSTX Upgrade where $I_{\rm p}$ is projected to reach 2 MA.

The pedestal width Δ is found to scale as $\Delta = c\sqrt{\beta_\theta^{\rm ped}}$ ($c = 0.17$ in NSTX) exhibiting qualitative similarity with the EPED model, and the DIIID [10] ($c = 0.06$) and MAST [14] ($c = 0.13$) experimental observations. The general width scaling with $\sqrt{\beta_\theta^{\rm ped}}$ is consistent with the barrier expansion phenomenology and shows that in ST this expansion is more pronounced than higher aspect-ratio tokamaks such as DIIID. The characterization of the pedestal parameters during an ELM cycle provides a good description of the NSTX ELMy regimes over a wide range of plasma currents and will be used for future tests of predictive pedestal models, such as EPED.

We examined the density fluctuations measured at the plasma edge during multiple ELM cycles using a 16-channel reflectometer. We observed large coherent fluctuations (near 12 kHz) increasing at the very edge of the plasma and away from the maximum density gradient. The coherent fluctuation decreases prior to the onset of the ELM cycle and is not observed in Mirnov spectrograms (suggesting that the coherent peak might be electrostatic). In summary, the behaviour of the density fluctuations suggests that they are less likely to play a role in constraining the profile gradients inside the edge barrier as the pedestal builds up.

The above experimental studies of the dynamic of pedestal parameters over a wide engineering parameter space provide predictions on the performance of NSTX U. For instance, increase of the pedestal height and broadening of the pedestal width with $I_{\rm p}$ will yield a factor 2.7 increase in the total pedestal pressure for NSTX U as well as a significant rise in the pedestal width, which will be manifested in higher pedestal stored energy. In addition to the predictive capability of next generation ST, results from these studies will be used for testing the pedestal structure predictive models which will be the subject of future papers.

Acknowledgments

NSTX team is gratefully acknowledged. A.D. acknowledges fruitful discussions with P. Snyder and encouragements from R. Nazikian. The authors would like to thank the referees for their constructive comments. This manuscript has been authored by Princeton University and collaborators under Contract Numbers DE-AC02-09CH11466, DE-AC05-00OR22725, DE-FG03-99ER54527, DE-FC02- 04ER54698, and DE-FG02-99ER54524 with the U.S. Department of Energy.

References

[1] ITER Physics Basis Editors 1999 *Nucl. Fusion* **39** 2137
[2] Loarte A. *et al* 2008 *Proc. 22nd Int. Conf. on Fusion Energy 2008 (Geneva, Switzerland, 2008)* (Vienna: IAEA) http://www-naweb.iaea.org/napc/physics/FEC/FEC2008/html/index.htm
[3] Osborne T.H. *et al* 1998 *Plasma Phys. Control. Fusion* **40** 845
[4] Urano H. *et al* 2002 *Nucl. Fusion* **42** 311
[5] Mukhovatov V. *et al* 2003 *Nucl. Fusion* **43** 942
[6] Shimada M. *et al* 2007 Progress in the ITER physics basis chapter 1: Overview *Nucl. Fusion* **47** S1
[7] Maggi C.F. 2010 *Nucl. Fusion* **50** 0660001
[8] Connor J.W., Hastie R.J., Wilson H.R. and Miller R.L. 1998 *Phys. Plasmas* **5** 2687
[9] Kirk A. *et al* 2004 *Phys. Rev. Lett.* **92** 245002
[10] Groebner R. *et al* 2009 *Nucl. Fusion* **49** 085037
[11] Snyder P.B., Groebner R.J., Leonard A.W., Osborne T.H. and Wilson H.R. 2009 *Phys. Plasmas* **16** 056118
[12] Maggi C. *et al* 2010 *Nucl. Fusion* **50** 025023
[13] Urano H. *et al* 2008 *Nucl. Fusion* **48** 045008
[14] Kirk A. *et al* 2009 *Plasma Phys. Control. Fusion* **51** 065016
[15] Maingi R. *et al* 2005 *Nucl. Fusion* **45** 1066
[16] Cordey J. *et al* 2003 *Nucl. Fusion* **43** 670
[17] Maingi R., Tritz K., Fredrickson E., Menard J. and Sabbagh S. 2005 *Nucl. Fusion* **45** 264
[18] Kugel H. *et al* 2009 *J. Nucl. Mater.* **390–391** 1000
[19] Bell M.G. *et al* 2009 *Plasma Phys. Control. Fusion* **51** 124054
[20] Canik J.M. *et al* 2010 *Phys. Rev. Lett.* **104** 045001
[21] Maingi R. *et al* 2009 *Phys. Rev. Lett.* **103** 075001
[22] Sontag A. *et al* 2011 Pedestal characterization and stability of small-ELM regimes in NSTX *Nucl. Fusion* at press
[23] Leblanc B.P. *et al* 2003 *Rev. Sci. Instrum.* **74** 1659
[24] Bell R.E. *et al* 2010 *Phys. Plasmas* **17** 082507
[25] Osborne T.H. *et al* 2008 *J. Phys.: Conf. Ser.* **123** 012014
[26] Groebner R.J. and Osborne T.H. 1998 *Phys. Plasmas* **5** 1800
[27] Gohil P. *et al* 1988 *Phys. Rev. Lett.* **14** 1603
[28] Wesson J.A. 1978 *Nucl. Fusion* **18** 87
[29] Manickam J. 1992 *Phys. Fluids* B **4** 1901
[30] Hegna C.C., Connor J.W., Hastie R.J. and Wilson H.R. 1996 *Phys. Plasmas* **3** 584
[31] Kirk A. *et al* 2007 *Plasma Phys. Control. Fusion* **49** 1259
[32] Maggi C. *et al* 2007 *Nucl. Fusion* **47** 535
[33] Groebner R.J., Osborne T.H., Leonard A.W. and Fenstermacher M.E. 2009 *Nucl. Fusion* **49** 045013
[34] Diamond P.H., Lebedev V.B., Newman D.E. and Carreras B.A. 1995 *Phys. Plasmas* **2** 3685
[35] Malkov M.A. and Diamond P.H. 2008 *Phys. Plasmas* **15** 122301
[36] Burckhart A. *et al* 2010 *Nucl. Fusion* **52** 105010
[37] Snyder P.B., Wilson H.R., Osborne T.H. and Leonard A.W. 2004 *Plasma Phys. Control. Fusion* **46** A131
[38] Snyder P. *et al* 2009 *Nucl. Fusion* **49** 085035
[39] Snyder P.B., Groebner R.J., Leonard A.W., Osborne T.H. and Wilson H.R. 2009 *Phys. Plasmas* **16** 056118
[40] Hughes J.W., Mossessian D.A., Hubbard A.E., Labombard B. and Marmar E.S. 2002 *Phys. Plasmas* **9** 3019
[41] Lingertat J. *et al* 1999 *J. Nucl. Mater.* **266–269** 124
[42] Saibene G. *et al* 1999 *Nucl. Fusion* **39** 1133
[43] Wilson H.R., Snyder P.B., Huysmans G.T.A. and Miller R.L. 2002 *Phys. Plasmas* **9** 1277
[44] Snyder P.B. *et al* 2002 *Phys. Plasmas* **9** 2037

[45] Snyder P. 1999 Gyrofluid theory and simulation of electromagnetic turbulence and transport in tokamak plasmas *PhD Thesis* Princeton University

[46] Belli E.A. and Candy J. 2010 *Phys. Plasmas* **17** 112314

[47] Crocker N.A., Peebles W.A., Kubota S., Zhang J. and Fredrickson E.D. 2010 High resolution MHD mode structure measurements via multichannel reflectometry in NSTX *52nd Annual Meeting of the DPP-APS 2010 (Chicago, Illinois, 8–12 November 2010)* http://meetings.aps.org/link/BAPS.2010.DPP.BP9.58

[48] Nazikian R., Kramer G.J. and Valeo E. 2001 *Phys. Plasmas* **8** 1840

[49] Diallo A. and Skiff F. 2005 *Phys. Plasmas* **12** 110701